Geophysical Research Letters®

Key Points:
- Terrestrial radar interferometry and GNSS identify dynamic changes at Priestley Glacier, Antarctica, forced by diurnal ocean tides
- Horizontal displacements vary semi-diurnally, are strongest in the shelf and decay near-linearly >10 km upstream of the grounding line
- Grounding line migration is small and flexural softening in ice-shelf shear margins can explain the semi-diurnal ice flow component

Grounding-Zone Flow Variability of Priestley Glacier, Antarctica, in a Diurnal Tidal Regime

R. Drews[1] , C. T. Wild[2,3] , O. J. Marsh[4] , W. Rack[3] , T. A. Ehlers[1] , N. Neckel[5] , and V. Helm[5]

[1]Department of Geosciences, Tübingen University, Tübingen, Germany, [2]College of Earth, Ocean, and Atmospheric Sciences, Oregon State University, Corvallis, OR, USA, [3]Gateway Antarctica, Canterbury University, Christchurch, New Zealand, [4]British Antarctic Survey, Cambridge, UK, [5]Helmholtz Centre for Polar- and Marine Research, Alfred Wegener Institute, Bremerhaven, Germany

Abstract Tidal modulation of ice streams and their adjacent ice shelves is a real-world experiment to understand ice-dynamic processes. We observe the dynamics of Priestley Glacier, Antarctica, using Terrestrial Radar Interferometry (TRI) and GNSS. Ocean tides are predominantly diurnal but horizontal GNSS displacements also oscillate semi-diurnally. The oscillations are strongest in the ice shelf and tidal signatures decay near-linearly in the TRI data over >10 km upstream of the grounding line. Tidal flexing is observed >6 km upstream of the grounding line including cm-scale uplift. Tidal grounding line migration is small and <40% of the ice thickness. The frequency doubling of horizontal displacements relative to the ocean tides is consistent with variable ice-shelf buttressing demonstrated with a visco-elastic Maxwell model. Taken together, this supports previously hypothesized flexural ice softening in the grounding-zone through tides and offers new observational constraints for the role of ice rheology in ice-shelf buttressing.

Plain Language Summary Temperatures in Antarctica's interior are below zero, so that ice continuously accumulates through snowfall. This mass gain is balanced by ice transport from the interior toward the coast. There, floating ice shelves form on the ocean and ice is eventually lost through iceberg calving and ocean induced melting. Small changes in any of these processes impact global ocean circulation and mean sea level. The speed of the ice varies with ocean tides. We use a specialized instrument that detects this variability and tidal flexing area-wide and every few hours. We find that although low- and high-tide only occur once a day in this area, ice flow is largest twice a day. This can be explained because ice softens when it is flexed by the ocean tides so that it can flow episodically faster. This is important because the deformation of ice shelves determines to an extent the stability of the entire ice sheet.

1. Introduction

The mass budget of Antarctica is controlled by a network of ice streams draining from the Antarctic plateau toward the ocean. At the grounding line, floating ice shelves are formed where ice is lost through basal melting and iceberg calving. Ice dynamics are modulated by ocean tides (Rosier et al., 2017), providing a rigorous test case for processes controlling ice discharge (Padman et al., 2018). Relevant processes include elastic and viscous stress transmission across the grounding line (Thompson et al., 2014), changing subglacial hydrology (Rosier & Gudmundsson, 2016), changing ice-shelf buttressing (Rosier & Gudmundsson, 2018), temporal ungrounding (Minchew et al., 2017), as well as imprints in sediment flow and till strength (Christianson et al., 2013; Walker et al., 2013). All of these processes are poorly constrained by observations, yet important for model projections of Antarctic ice discharge.

Tides influence both the horizontal and vertical ice flow components. In the Rutford (Gudmundsson, 2006; Minchew et al., 2017) or Beardmore ice streams (Marsh et al., 2013), for example, horizontal flow is modulated most strongly on fortnightly spring-to-neap frequencies, suggesting that these ice streams respond non-linearly to peak-to-peak changes in tidal amplitudes. Other ice streams, for example, the Bindschadler ice stream (Anandakrishnan et al., 2003) do not show this behavior and vary in-phase with the prevailing tides. For glaciers feeding into the Ronne Ice Shelf, tidal modulation persists more than 80 km upstream of the grounding line (Rosier et al., 2017). In areas with smaller tidal amplitudes, tidal signatures are not

seen at all (Scott et al., 2009) or up to only a few kilometers upstream of the grounding line (Heinert & Riedel, 2007). Advanced visco-elastic models have resulted in much progress in understanding this contrasting behavior (Rosier & Gudmundsson, 2020; Thompson et al., 2014). Yet, there are still significant differences in how tides are incorporated into ice-sheet models (Rosier & Gudmundsson, 2016), and all models require a high degree of tuning to match observations. Flexural bulging (Walker et al., 2013) or elastic peeling (Warburton et al., 2020) can move ocean water landwards, changing the local hydrology (Begeman et al., 2020; Milillo et al., 2019) and till properties (Christianson et al., 2013). Thus far, however, only a few ground-based observations (Heinert & Riedel, 2007; Smith, 1991) provide direct observational support for vertical deflections upstream of the grounding line.

Synthesis of a densely spaced satellite time series on Rutford Ice Stream has shown that the ice shelf leads the tidal response, which is then communicated with a phase-lag through the grounding zone into the ice stream (Minchew et al., 2017). Tidally induced grounding-line migration and ephemeral grounding during low-tide have been suggested as a possible mechanism (Minchew et al., 2017; Robel et al., 2017; Rosier & Gudmundsson, 2020). Indicators for this are low ice velocities during low-tide. The non-linear ice rheology can cause flexural softening of the ice in the grounding zone both during high- and low-tide. This would manifest itself in ice-shelf velocities modulated at frequencies double of the underlying tidal forcing (Rosier & Gudmundsson, 2018). However, so far there has been no clear observational evidence for this.

We extend this line of research with new observations at the grounding zone of Priestley Glacier, a deeply incised and heavily buttressed valley glacier draining ice through the Transantarctic Mountains into the Nansen Ice Shelf. As shown in more detail below, surface velocities average ~160 m a^{-1}, ice thickness is ~1,200 m, and the ice-bed interface is >500 m below sea level for >80 km inland. Tides are predominantly diurnal with amplitudes of ±0.5 m. Priestley Glacier provides a unique opportunity to study the upstream signal propagation of ocean tides, because an ice-free ridge elevated 1,000 m above the glacier surface provides a firm anchor and a good viewpoint for a Terrestrial Radar Interferometer (TRI, Figure 1a). TRI has been applied previously in Greenland (Xie et al., 2018) but not in Antarctica where logistical constraints are larger. With a TRI grounding-zone flexure and ice-flow can be imaged on hourly timescales. In combination with GNSS and a visco-elastic model, we use this to understand how the Priestley Glacier system is modulated by tides and if the underlying mechanism originates at the grounding line, in the ice stream or in the ice shelf. A secondary objective is to understand if flexural bulging occurs upstream of the grounding line with corresponding impacts for grounding zone stability.

2. Methods

2.1. Derivation of Line-of-Sight Velocities and Grounding Zone Flexure Using Terrestrial Radar Interferometry

TRI data were acquired using a Gamma Remote Sensing Portable Radar Interferometer (GPRI-2). Images were acquired at 3 min intervals and gridded to 10 m postings, which is the approximate azimuthal resolution for a distance of 1 km (Caduff et al., 2015). Ice speed was mapped every 0.5 hr in a line-of-sight (LOS) geometry using standard satellite interferometry techniques (Text S1 in Supporting Information S1). Each LOS velocity field results from multi-temporal stacking of ~50 unwrapped interferograms with a minimum temporal baseline of 2.8 hr in a 3-hr time period. Stacking is applied to reduce random instrument noise and atmospheric variability over timescales shorter than the stacking interval. This results in residual random velocities at the ice-free rock walls within the scene, typically <10% of the glacier velocities.

The projection between TRI LOS velocity ($v_{LOS} > 0$ for movement toward the sensor) is given by the dot-product from the radar look-vector with the GNSS glacier velocity vector $\mathbf{v} = (v_x, v_y, v_z)$:

$$v_{LOS}(t_1, t_2) = \underbrace{\sin(\phi)\cos(\theta)}_{s_x} v_x(t_1, t_2) + \underbrace{\sin(\phi)\sin(\theta)}_{s_y} v_y(t_1, t_2) + \underbrace{\cos(\theta)}_{s_z} v_z(t_1, t_2) \tag{1}$$

where ϕ and θ are the azimuthal orientation and local incidence angles, respectively. This results in differing sensitivities (s_x, s_y, s_z) of TRI to horizontal and vertical velocity components. For our geometry, the sensitivity is lowest for v_z and varies for v_x (approx. across-flow) and v_y (approx. along-flow) across the scene (Figure S1 in Supporting Information S1).
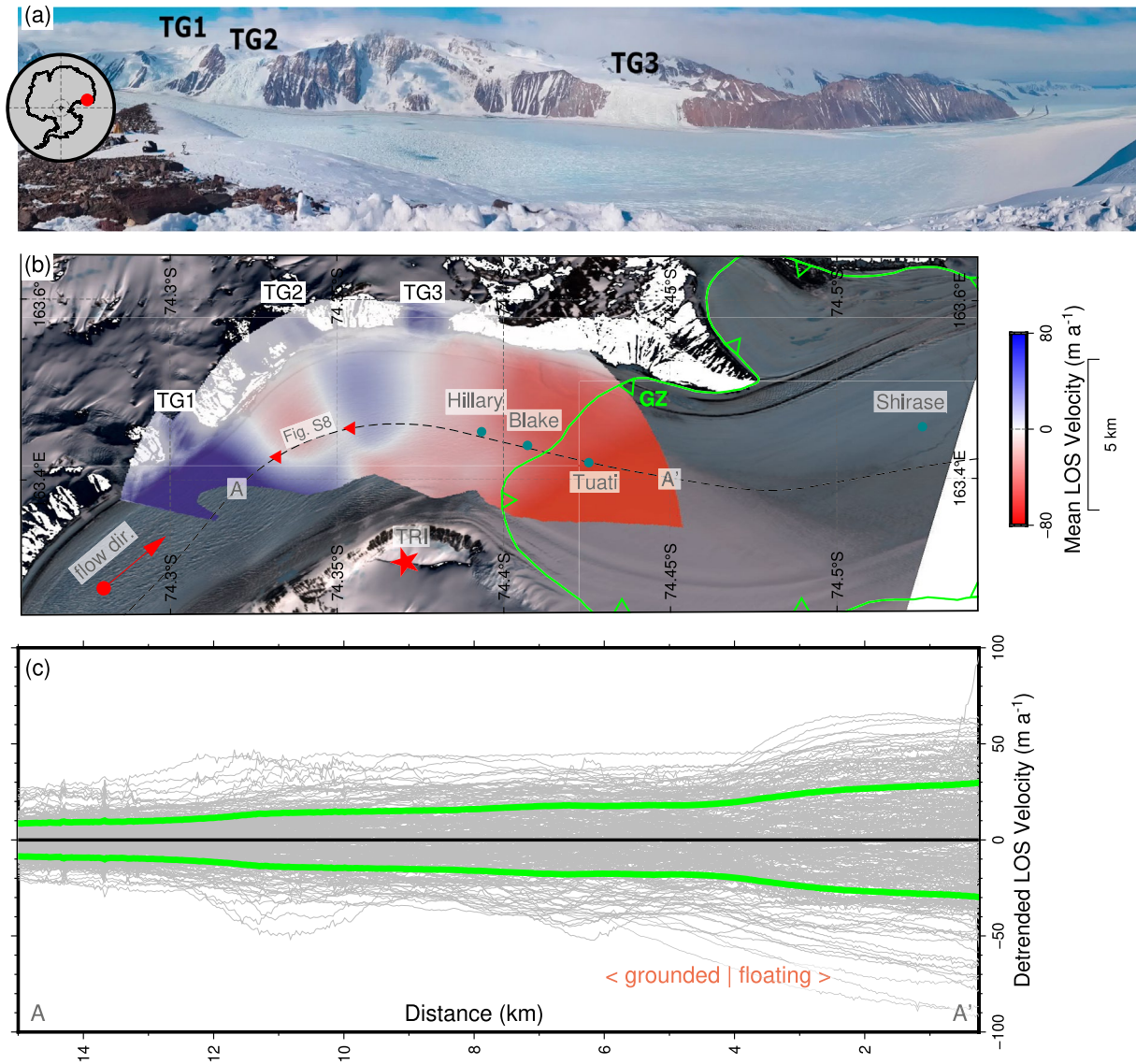
Figure 1. (a) Panoramic view from TRI location overlooking Priestley Glacier with three marked tributary glaciers (TG 1–3). Ice flow direction is from left (north) to right (south). (b) Mean ice flow in the line-of-sight (LOS) direction with positive values marking ice movement toward the TRI. Hillary, Blake and Tuati are GNSS stations. Red triangles mark Bull's eye location referred to in the main text and Figure S12 in Supporting Information S1. The estimated landward limit of the grounding zone (GZ) is shown with a yellow curve. Background image is acquired by Sentinel 2. (c) Deviation from the mean of ice flow along A-A' over an 8 day period. Gray curves are taken approximately every 0.5 hr and each curve represents a temporal average over 3h. Green curves mark ± one standard deviation.

Tidal flexure and velocity variability were quantified by differencing individual interferograms with a common temporal baseline Δt formed out of image triplets collected at times t_1, t_2, and t_3:

$$v_{LOS}(t_1,t_2) - v_{LOS}(t_2,t_3) = \frac{1}{\Delta t}\Big(s_x(2x_2 - x_1 - x_3) + s_y(2y_2 - y_1 - y_3) + s_z(2z_2 - z_1 - z_3)\Big) \qquad (2)$$

where the $x_{\{1,2,3\}}, y_{\{1,2,3\}}, z_{\{1,2,3\}}$ represent the x, y, and z positions in the acquisitions at times t_1, t_2, and t_3. Differencing interferograms cancels the mean glacier flow and highlights modulation by tides (Rignot, 1996). The dense spacing of TRI acquisition enables differential interferometry without stacking and at intervals of 3 min.

2.2. Detecting Flow Variability With GNSS

GNSS data at the four stations Shirase, Tuati, Blake, and Hillary cover a longer time period than the TRI and are located in Figure 1b. Positions were computed with Precise Point Positioning. Vertical and horizontal velocities were obtained from the slope of a linear regression over a minimum of 6 hr corresponding to a maximum horizontal displacement of ≪10 cm. For the 12 hr time differences applied in the differential interferometry, the solutions are at the detection limit as the predicted differential vertical displacement is within a few centimeters (Text S2 in Supporting Information S1).

2.3. Principal Component Analysis for the TRI Time Series

To isolate the underlying spatial and temporal patterns in the TRI data, principal component analysis is applied to the demeaned time series of $N = 288$ TRI LOS velocity fields, each of them gridded to a raster with dimensions $n \times m$. This results in a decomposition of the TRI LOS velocity field $\mathbf{V}_{LOS}^i$ at time $i = 1..N$, into a new set of $n \times m$ basis fields termed principal components ($\mathbf{PC}_j, j = 1..N$):

$$\mathbf{V}_{LOS}^i = \bar{\mathbf{V}}_{LOS} + \sum_{j=1}^{N} a_j^i \mathbf{PC}_j. \tag{3}$$

Here, $\bar{\mathbf{V}}_{LOS}$ is the temporally averaged TRI LOS velocity field and a_j^i represents the weights of $\mathbf{PC}_j$ for reconstructing the flowfield at time i. The a_j^i are normalized relative to $max(a_1^i)$ so that they range between -1 and 1. They are sorted so that the explained variance decreases with increasing j. The first two $\mathbf{PC}_{1,2}$ explain 78% (=65% + 13%) of the total variance and have a spatial pattern that can be meaningfully interpreted. Time series analysis of $a_{1,2}^i$ determines the relevant frequencies for $\mathbf{PC}_{1,2}$ and provide the temporal context of tidal signal propagation upstream of the grounding line.

2.4. Detecting the Extent of the Grounding Zone

Using terminology from satellite observations (Fricker et al., 2009), the grounding zone extends between the freely floating point H and hinge line F where no vertical deflection occurs. This is slightly upstream of the grounding line G, which we locate in an ice-penetrating radar transect from 2013 (Paden et al., 2010) using an abrupt change in basal reflectivity (Figure S12 in Supporting Information S1). The points F and H are approximated using differential interferometry (Rignot, 1996) to a set of 17 differential Sentinel 1 and TerraSAR-X interferograms (Figures S10 and S11 in Supporting Information S1). Both satellites have at least one acquisition in November 2018 concurrent to the in-situ measurements (Text S3 in Supporting Information S1). In this context, the GNSS station Shirase is seawards of H and freely floating, Tuati is located at the grounding line approximately 1 km downstream of F. Blake is at or slightly upstream of F on grounded ice. Hillary is upstream of F (Figure 1).

2.5. Modeling Ice-Shelf Displacement With Tidally Modulated Buttressing

Qualitative patterns in detrended ice-shelf displacement are investigated with a depth-integrated, lumped Maxwell model for a visco-elastic beam subject to average stresses partitioned into hydrostatic stresses (σ_{h0}), buttressing stresses (σ_{b0}), and other background stresses. This model has been applied previously to Rutford and Bindschadler ice streams (Robel et al., 2017). The dependency of buttressing stresses on tides is inferred from the observed relationship between strain and tidal height. In previous examples, the strain-height parameterization was consistent with variable buttressing induced by tidal grounding-line migration (Robel et al., 2017). As shown below, the TRI inferred grounding line for Priestley Glacier is virtually stagnant, and also the strain-tidal height relationship is different as high strain between Tuati and Shirase is observed both during low- and high-tide (Figure S13 in Supporting Information S1). To account for this, the model is modified and hereafter referred to as mAR17. The modification includes a new parameterization of the buttressing stresses replacing Equation 5 in Robel et al., 2017 with:

$$\sigma_b = \beta(0.5h^\alpha - 0.2). \tag{4}$$
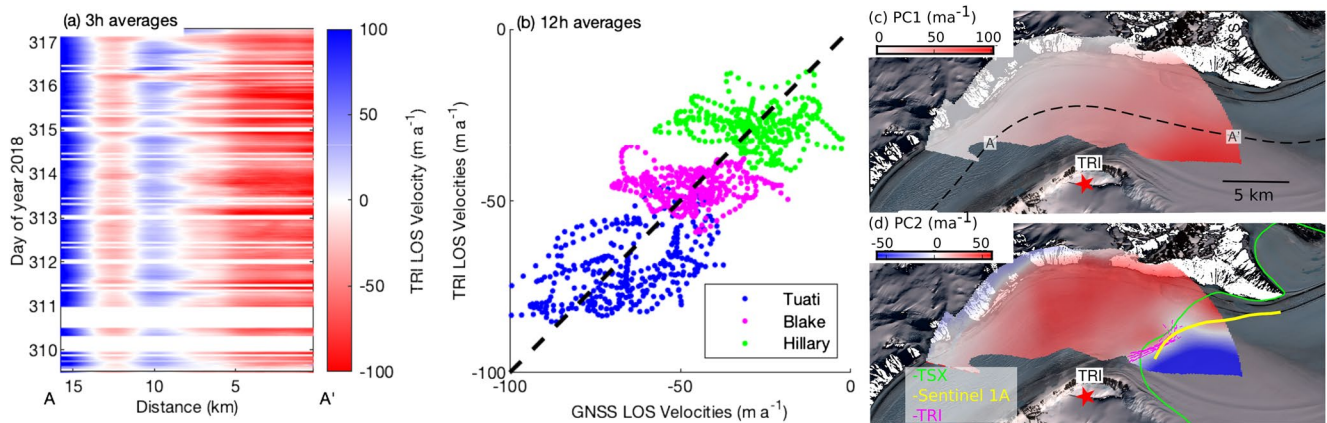
Figure 2. (a) Time series of 3-hr TRI flowfields along profile A-A′ compared in (b) Over 12 hr intervals with GNSS data projected into line-of-sight (LOS). Panels (c) and (d) show the principal components 1 and 2 of the TRI time series jointly explaining 78% of the total variance in the entire data set. Estimates for the landward limit of the grounding zone from TerraSAR-X, Sentinel-1 and TRI are shown with green, yellow, and magenta curves, respectively.

β is the ratio between the magnitude of change for buttressing and hydrostatic stresses, h is the tidal displacement, $\alpha = 2.0$ determines the non-linearity in ice-shelf buttressing and is inferred from the strain-tidal height data, $\sigma_{h0} = 5\,\text{kPa}$ is chosen consistently with $h \sim 0.5\,\text{m}$. β is treated as a free parameter alongside with γ describing the ratio between background and hydrostatic stresses (Text S5 in Supporting Information S1).

3. Results

3.1. Temporally Persistent LOS Flowfield Patterns

The mean LOS velocity field (Figure 1b) captures the ice-stream dynamics in several ways. First, the North-South directed ice flow is represented in the LOS velocity field with positive values (i.e., movement toward the sensor) on the upstream side and with negative values (i.e., movement away from the sensors) at the downstream side. Second, sensitivity is lowest to the along-flow direction in the scene center, explaining the comparatively low LOS velocity values there. Third, the three tributary glaciers flowing into the main trunk of Priestley Glacier (TG1-TG3) are all detected and ice free rock walls show negligible velocity signals. Fourth, in the upstream section the LOS velocity exhibits an oscillation termed a Bull's eye pattern (Figure 1b). It occurs in an area of localized surface depressions, resulting in closed phase contours in corresponding interferograms (Figure S2 in Supporting Information S1).

3.2. Temporally Variable Flowfield Patterns and Frequency Doubling

At the grounding line near Tuati, vertical velocities are highest ($\sim$170 m a^{-1}) at rising tides and lowest at falling tides ($\sim$130 m a^{-1}). Horizontal velocities are slowest ($\sim$80 m a^{-1} during rising tides and fastest ($\sim$175 m a^{-1}) during falling tides (Figure S3 in Supporting Information S1). This relationship is weaker but still significant further upstream on grounded ice (i.e., at Blake i Figure S4 in Supporting Information S1).

The TRI time series (Figure 2a) compares well in average with the GNSS derived velocities over 12 hr and longer timescales (Figure 2b), showing that projection of the GNSS data into LOS is meaningful. Particularly at stations Hillary and Blake, however, the comparison deteriorates over shorter timescales because noisy GNSS positions results in spurious velocities. At Tuati, 6 hr velocities still compare well with the TRI within 3 ± 20 m a^{-1} in mean and standard deviation for a LOS velocity bracketing 30–110 m a^{-1} (Figures S3a–S3d in Supporting Information S1). Interpretation of the TRI data needs to account for that projection into LOS mixes vertical and horizontal velocities with differing sensitivities, and that all of these components are significantly modulated by tides.

The principal components of the TRI time series (Figures 2c and 2d) describe the spatiotemporal signature of tidal ice-flow modulation at and upstream of the grounding line. **PC1** exhibits a near-linear ramp decaying in magnitude with increasing distance from the grounding line, similar to the decaying variability
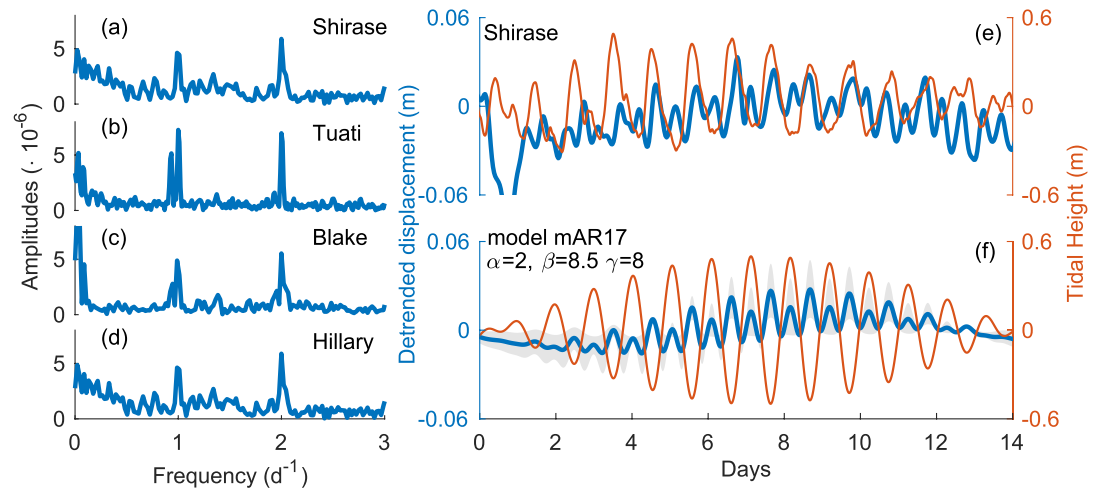
Figure 3. Spectrum from the detrended horizontal GNSS displacement at Shirase (a), Tuati (b), Blake (c) and Hillary (d). These stations are located in Figure 1 and all show a semi-diurnal and diurnal frequency peaks in a predominantly diurnal tidal regime. Detrended horizontal displacement at Shirase is shown with measured vertical displacement in panel (e) and has similar patterns as the modeling output (f) including the observed frequency doubling between tides and horizontal displacement. The gray background indicates the spread in model predictions for a range of buttressing encompassing 5–80 kPa corresponding to $\beta = 1$–16.

in Figure 1c. The corresponding weight a_1 has its extremal values close to the rising and falling tides. **PC2** has patterns of changing polarity with zero crossing close to the hinge line (Figure S8 in Supporting Information S1). Maxima in a_2 are approximately 90° phase shifted relative to a_1. The principal components are interpreted later as proxy for tidal ice-flow modulation and flexure.

Tidal harmonic analysis (Pawlowicz et al., 2002) of the horizontal displacement in the longer-term GNSS data reveal additional dynamics, which are not immediately apparent in the shorter-term TRI time series or the regression to GNSS velocities. This includes higher-frequency variability that is masked by the 6–12 hr regression required to go from displacement to velocities. Shirase show fortnightly cycles on the ice shelf, which also occurs with smaller amplitude at the grounding line (Figures S8a and S8b in Supporting Information S1). This low-frequency oscillation is paired with diurnal and semi-diurnal variability that also occurs in the ice stream (Figures 3a–3d; Figures S8c and S8d in Supporting Information S1). Vertical displacements at Shirase and Tuati, on the other hand, are predominantly diurnal (Figure 3e).

The observed semi-diurnal frequency doubling in a diurnal tidal regime is a novel finding that is qualitatively reproduced in mAR17 with the new parameterization of the buttressing stresses (Figure 3f). Effectively this parameterization modulates ice-shelf buttressing during high- and low-tide mimicking flexural softening which is most important during the largest ice-shelf deflection (Rosier & Gudmundsson, 2018). We will discuss this further after the investigation of grounding-zone flexure patterns.

3.3. Tidal Flexure Patterns

For the tidal flexure analysis, we choose a temporal baseline $\Delta t = 12$ h, which maximizes the double differential signal for the diurnal tidal components. Two unwrapped time steps are shown here in Figures 4a and 4b, and the full time series of differential interferograms is provided in Movie S1. Using the GNSS data, we disentangle which components of the differential 3D displacement are mapped into the LOS geometry at the respective location.

At Tuati, the TRI viewing geometry is such that the sensitivity toward the differential vertical component is low ($s_z \approx 0.1$), and the sensitivity toward the differential horizontal components is high ($s_x \approx s_y \approx 0.7$). After the projection into LOS, the differential GNSS data fit to the differential TRI data at the cm-level (Figures S3e and S3f in Supporting Information S1). The two differential horizontal components are as large as the differential vertical components. Coincidentally both of them average out at that specific location, so
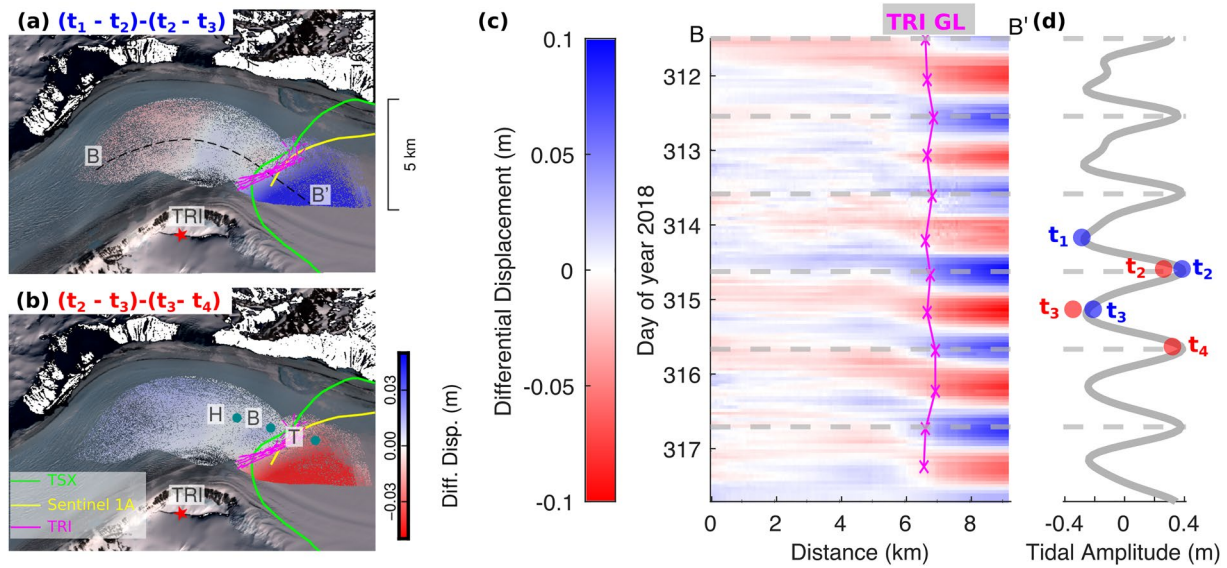
Figure 4. Differential displacement fields for image triplets covering a low-tide to low-tide (a) and a high-tide to high-tide (b) cycle. Landward limit of the grounding zone as estimated with TerraSAR-X (green), Sentinel-1 (yellow) and the TRI (magenta) interferometry. The full differential time series along transect B-B′ (located in panel a) is shown in panel (c) in relation to the predicted tidal amplitudes (Padman et al., 2002; d).

that it serves as a proxy for the hinge line F which we pick for 12 successive tidal cycles (Figures 4a and 4b). The picks differ in most areas <500 m (or <40 % of the local ice thickness), which is too small to coherently assign it to individual tidal cycles (Figure 4c). The grounding-line of Priestley Glacier thus appears to be pinned to the bed, and we contextualize these findings later with satellite based estimates.

At Blake, the TRI viewing geometry is similar to Tuati, and the differential GNSS data equally reproduce the differential TRI observations (Figure S5 in Supporting Information S1). Interestingly, while vertical deflection at Tuati is synchronous with tides, Blake exhibits signatures of uplift twice in a single high-tide to low-tide transition (Figures S5c and S7 in Supporting Information S1). This vertical deflection is at the cm-limit and differs between different GNSS processing schemes, yet neglecting it results in a worse fit to the TRI data. Uplift landwards of G during low-tide would be consistent with existence of a fulcrum at G leveraging vertical displacement that is in anti-phase with tides. Farther upstream, no significant flexure pattern is detected in the GNSS data (Figure S6 in Supporting Information S1). The differential TRI data, however, reveal coherent flexure patterns >6 km upstream of H over all tidal cycles (Figure 4c).

4. Discussion

The TRI data delivers a spatio-temporal time series of grounding-zone dynamics that can be matched with GNSS derived velocities and differential displacements on sub-daily timescales. This shows that TRI detects ice-dynamic modulations on tidal timescales and at cm-resolution even in areas where the viewing geometry is not favorable. An example is the Bull's eye pattern. Similar patterns have been observed in satellite interferometry and were explained with ice flow over dynamically supported surface depressions (Joughin et al., 1995). This also applies here as the pattern is temporally persistent and occurs in an area of changing surface slope caused by ice flow over a basal obstacle (Figure S12 in Supporting Information S1). This results in lowering and then in re-emergence of the ice-flow vector that is readily detected by the TRI.

The wealth of data collected by the TRI can be efficiently reduced with principal component analysis. We interpret that **PC1** quantifies the upstream extent of tidal modulations which decay near-linearly with distance over >10 km. This linearity has also been observed at Rutford ice stream although the decay length there is with ~85 km significantly longer (Minchew et al., 2017). In parts, this is because tidal amplitudes at Priestley Glacier are a factor of six smaller than the amplitudes at Rutford ice stream. Spatial patterns in **PC1** show some across-flow variability where tidal signatures propagate more strongly on the ice stream's true right side (Figure 2c). The asymmetry is matched by the geometry of constraining mountain ranges.

This is consistent with decoupling from the true right shear zone and enables a longer transmission of tidal stresses (Thompson et al., 2014).

The observed fortnightly variability adds the Nansen Ice Shelf into a list of other ice shelves (Rosier et al., 2017), which are sensitive to the beat-frequency of the two main components in the prevailing tidal forcing (here between the K_1 and S_1 tidal components). The most recent explanation with a 3D visco-elastic full Stokes model has identified tidally induced grounding-line migration as a likely mechanism (Rosier & Gudmundsson, 2020). As detailed below, we observe a comparatively stagnant grounding-line for Priestley Glacier although grounding-line migration may still occur elsewhere on the ice shelf. Our time series is not long enough to probe how or if the fortnightly variability is communicated into the ice stream. A novel finding is the mixed diurnal and semi-diurnal components in the horizontal flow seen at all GNSS stations, despite the predominantly diurnal tidal regime. Shirase shows the clearest signal in this regard with larger displacements at times of low- and high-tide (Figure 3c and Figure S8a in Supporting Information S1). At Tuati, Blake, and Hillary, the two frequencies superimpose so that the resulting amplitudes are modulated throughout the respective time series (Figures S8b and S8d in Supporting Information S1). The diurnal variability on the ice-shelf has been linked previously to ice-shelf tilting (Rosier & Gudmundsson, 2020), ice-shelf buttressing (Robel et al., 2017), or bending of the ice surface (Rack et al., 2017; Wild et al., 2019). The semi-diurnal variability results in high-strain between Shirase and Tuati at times of high tidal deflection (Figure S13 in Supporting Information S1). Using a similar reasoning as Robel et al., 2017, we interpret this as a proxy for non-linear ice-shelf buttressing parameterized with Equation 3. The underlying process, however, must be different than what has been suggested previously as preferential grounding during low tide does not result in a frequency doubling. The latter is consistent with flexural softening in which the non-linear ice rheology weakens ice-shelf shear margins both during low- and high-tide (Rosier & Gudmundsson, 2018). This causes frequency doubling in addition to the diurnal variability from ice-shelf tilting or bending. It will be most relevant in areas where variability in the semi-diurnal buttressing stresses is larger than the variability in the diurnal hydrostatic stresses, meaning that $\beta \gg 1$ as shown in mAR17. This applies to Priestley Glacier because tidal amplitudes are small and buttressing is presumably large due to the tight lateral constraints. These observation add support to the hypothesis that ice dynamic modulation by tides originates near grounding zones (Minchew et al., 2017; Rosier & Gudmundsson, 2020), and further investigations can use this to test the role of the rheology in ice-shelf shear margins, for example, by including higher Glen exponents or ice anisotropy.

There are several implications from the analysis of the tidal flexure patterns. First, the observed double uplift at Blake resembles previous observations at Ekström Ice Shelf (Heinert & Riedel, 2007). The first uplift during high-tide can be caused by the adjacent ice shelf, and the second uplift during low-tide can be caused by local regrounding, resulting in an ephemeral fulcrum. The existence of a fulcrum is important, given that even cm-scale surface deflections have a significant impact on the subglacial hydrology (Begeman et al., 2020; Milillo et al., 2019; Walker et al., 2013; Warburton et al., 2020) and grounding zone stability (Christianson et al., 2013). Second, the flexure pattern observed more than 6 km upstream of the grounding line is predominantly horizontal given the low vertical TRI sensitivity. This provides a test-case to investigate tidally induced shortening/extension at the surface to further differentiate between viscous and elastic deformation (Rack et al., 2017; Wild et al., 2019). Third, horizontal velocities vary significantly over tidal cycles and in general do not cancel during double differencing. The pattern that is seen in differential interferometry is hence not only due to deformation in the vertical axis, making the delineation of the grounding-zone more difficult. Near simultaneous estimates of F from Sentinel 1 and TerraSAR-X agree with TRI in the ice-stream center where we have shown that the differential horizontal components cancel (Figure S3 in Supporting Information S1). Toward the true-left side, the coherence of the TRI interferograms deteriorates over a blue ice zone so that the landward limit of the tidal fringe pattern cannot unequivocally be identified making the delineation more subjective. In this area, the zero transition of **PC2** also deviates from the satellite-based estimates of F whereas it fits well in the ice-stream center. This indicates that away from the ice-stream center the TRI picks up some of the residual horizontal variability. This bias in F will be larger for TRI than for the satellites which are more sensitive to the vertical components because of steeper incidence angles (~10° for TRI vs 20° – 40° for satellites). On the other hand, the dense spacing of the TRI data allows to pick F at the tidal maxima where the vertical signal is strongest. Regardless of a potential bias, the location of F in the TRI time series varies <500 m, and the stability is further evidenced by **PC2** in

which the zero-transition coincides with the TRI estimate of H (Figure 2d). This means that although F is likely biased, only little migration occurs on tidal timescales. Satellite estimates of F show a larger spread over a 3-year time interval with differences of up to 2 km. However, there is no systematic trend (Figures S10 and S11 in Supporting Information S1), which suggests that at least some of the satellite derived variability in F is due to unresolved horizontal components. Whether or not residual horizontal velocities are maintained in differential interferograms in general will be site-specific and is depended on the viewing geometry. Checking for tidal variability prior to hinge line delineation is one way to account for this (Milillo et al., 2017).

5. Conclusion

We have deployed a Terrestrial Radar Interferometer surveying the grounding zone of Priestely Glacier subject to predominantly diurnal tides. We detect tidal ice-flow modulation which decays linearly >10 km upstream the grounding line. The horizontal modulations do not necessarily cancel in differential interferometry so that the resulting fringe patterns cannot unambiguously be linked to only vertical deflection. Horizontal flow on the ice shelf and the ice stream is also modulated on semi-diurnal periods consistent with flexural softening of ice-shelf shear margins. The observations are qualitatively replicated with a Maxwell model using a non-linear parameterization of ice-shelf buttressing with tides. Differential tidal flexure patterns reveal a pinned grounding line and local uplift upstream thereof indicating the existence of an ephemeral fulcrum. The projection from a 3D reference frame into the line-of-sight geometry of terrestrial radar interferometry is purely geometric and contains no tuning factors. This means that flowfield time series and the flexure patterns are a new observational benchmark that can be used to test ice-flow models in order to isolate the dominating processes of ice-stream mechanics.

Data Availability Statement

GNSS data are available at: https://doi.pangaea.de/10.1594/PANGAEA.936090. The differential displacement fields are available at: https://doi.pangaea.de/10.1594/PANGAEA.935707. The line-of-sight velocities are available at: https://doi.pangaea.de/10.1594/PANGAEA.935702.

References

Anandakrishnan, S., Voigt, D. E., Alley, R. B., & King, M. A. (2003). Ice stream D flow speed is strongly modulated by the tide beneath the Ross Ice Shelf. *Geophysical Research Letters*, *30*(7), 1361. https://doi.org/10.1029/2002GL016329

Begeman, C. B., Tulaczyk, S., Padman, L., King, M., Siegfried, M. R., Hodson, T. O., & Fricker, H. A. (2020). Tidal pressurization of the ocean cavity near an Antarctic ice shelf grounding line. *Journal of Geophysical Research: Oceans*, *125*(4), e2019JC015562. https://doi.org/10.1029/2019JC015562

Caduff, R., Schlunegger, F., Kos, A., & Wiesmann, A. (2015). A review of terrestrial radar interferometry for measuring surface change in the geosciences. *Earth Surface Processes and Landforms*, *40*(2), 208–228. https://doi.org/10.1002/esp.3656

Christianson, K., Parizek, B. R., Alley, R. B., Horgan, H. J., Jacobel, R. W., Anandakrishnan, S., et al. (2013). Ice sheet grounding zone stabilization due to till compaction. *Geophysical Research Letters*, *40*(20), 5406–5411. https://doi.org/10.1002/2013GL057447

Fricker, H. A., Coleman, R., Padman, L., Scambos, T. A., Bohlander, J., & Brunt, K. M. (2009). Mapping the grounding zone of the Amery Ice Shelf, East Antarctica using InSAR, MODIS and ICESat. *Antarctic Science*, *21*(05), 515–532. https://doi.org/10.1017/S095410200999023X

Gudmundsson, G. H. (2006). Fortnightly variations in the flow velocity of Rutford Ice Stream, West Antarctica. *Nature*, *444*(7122), 1063–1064. https://doi.org/10.1038/nature05430

Heinert, M., & Riedel, B. (2007). Parametric modelling of the geometrical ice-ocean interaction in the Ekstroemisen grounding zone based on short time-series. *Geophysical Journal International*, *169*(2), 407–420. https://doi.org/10.1111/j.1365-246X.2007.03364.x

Joughin, I. R., Winebrenner, D. P., & Fahnestock, M. A. (1995). Observations of ice-sheet motion in Greenland using satellite radar interferometry. *Geophysical Research Letters*, *22*(5), 571–574. https://doi.org/10.1029/95GL00264

Marsh, O. J., Rack, W., Floricioiu, D., Golledge, N. R., & Lawson, W. (2013). Tidally induced velocity variations of the Beardmore Glacier, Antarctica, and their representation in satellite measurements of ice velocity. *The Cryosphere*, *7*(5), 1375–1384. https://doi.org/10.5194/tc-7-1375-2013

Milillo, P., Rignot, E., Mouginot, J., Scheuchl, B., Morlighem, M., Li, X., & Salzer, J. T. (2017). On the short-term grounding zone dynamics of Pine Island Glacier, West Antarctica, observed with COSMO-SkyMed interferometric data: PIG grounding line dynamics. *Geophysical Research Letters*, *44*(20), 10,436–10,444. https://doi.org/10.1002/2017GL074320

Milillo, P., Rignot, E., Rizzoli, P., Scheuchl, B., Mouginot, J., Bueso-Bello, J., & Prats-Iraola, P. (2019). Heterogeneous retreat and ice melt of Thwaites Glacier, West Antarctica. *Science Advances*, *5*(1), eaau3433. https://doi.org/10.1126/sciadv.aau3433

Minchew, B. M., Simons, M., Riel, B., & Milillo, P. (2017). Tidally induced variations in vertical and horizontal motion on Rutford Ice Stream, West Antarctica, inferred from remotely sensed observations. *Journal of Geophysical Research: Earth Surface*, *122*(1), 167–190. https://doi.org/10.1002/2016JF003971

Paden, J., Li, J., Rodriguez-Morales, F., & Hale, R. (2010). *IceBridge MCoRDS L2 Ice Thickness, version 1*. NASA National Snow And Ice Data Center Distributed Active Archive Center. https://doi.org/10.5067/GDQ0CUCVTE2Q

Padman, L., Fricker, H. A., Coleman, R., Howard, S., & Erofeeva, L. (2002). A new tide model for the Antarctic ice shelves and seas. *Annals of Glaciology*, *34*, 247–254. https://doi.org/10.3189/172756402781817752

Padman, L., Siegfried, M. R., & Fricker, H. A. (2018). Ocean tide influences on the Antarctic and Greenland ice sheets: Tide influences on ice sheets. *Reviews of Geophysics*, *56*(1), 142–184. https://doi.org/10.1002/2016RG000546

Pawlowicz, R., Beardsley, B., & Lentz, S. (2002). Classical tidal harmonic analysis including error estimates in MATLAB using T_tide. *Computers & Geosciences*, *28*(8), 929–937. https://doi.org/10.1016/S0098-3004(02)00013-4

Rack, W., King, M. A., Marsh, O. J., Wild, C. T., & Floricioiu, D. (2017). Analysis of ice shelf flexure and its InSAR representation in the grounding zone of the southern McMurdo Ice Shelf. *The Cryosphere*, *11*(6), 2481–2490. https://doi.org/10.5194/tc-11-2481-2017

Rignot, E. (1996). Tidal motion, ice velocity and melt rate of Petermann Gletscher, Greenland, measured from radar interferometry. *Journal of Glaciology*, *42*(142), 476–485. https://doi.org/10.1017/S0022143000003464

Robel, A. A., Tsai, V. C., Minchew, B., & Simons, M. (2017). Tidal modulation of ice shelf buttressing stresses. *Annals of Glaciology*, *58*(74), 12–20. https://doi.org/10.1017/aog.2017.22

Rosier, S. H. R., & Gudmundsson, G. H. (2016). Tidal controls on the flow of ice streams. *Geophysical Research Letters*, *43*(9), 4433–4440. https://doi.org/10.1002/2016GL068220

Rosier, S. H. R., & Gudmundsson, G. H. (2018). Tidal bending of ice shelves as a mechanism for large-scale temporal variations in ice flow. *The Cryosphere*, *12*(5), 1699–1713. https://doi.org/10.5194/tc-12-1699-2018

Rosier, S. H. R., & Gudmundsson, G. H. (2020). Exploring mechanisms responsible for tidal modulation in flow of the Filchner-Ronne Ice Shelf. *The Cryosphere*, *14*(1), 17–37. https://doi.org/10.5194/tc-14-17-2020

Rosier, S. H. R., Gudmundsson, G. H., King, M. A., Nicholls, K. W., Makinson, K., & Corr, H. F. J. (2017). Strong tidal variations in ice flow observed across the entire Ronne Ice Shelf and adjoining ice streams. *Earth System Science Data*, *9*(2), 849–860.

Scott, J. B. T., Gudmundsson, G. H., Smith, A. M., Bingham, R. G., Pritchard, H. D., & Vaughan, D. G. (2009). Increased rate of acceleration on Pine Island Glacier strongly coupled to changes in gravitational driving stress. *The Cryosphere*, *7*. https://doi.org/10.5194/tc-3-125-2009

Smith, A. (1991). The use of tiltmeters to study the dynamics of Antarctic ice-shelf grounding lines. *Journal of Glaciology*, *37*(125), 51–58. https://doi.org/10.3189/S0022143000042799

Thompson, J., Simons, M., & Tsai, V. C. (2014). Modeling the elastic transmission of tidal stresses to great distances inland in channelized ice streams. *The Cryosphere*, *8*(6), 2007–2029. https://doi.org/10.5194/tc-8-2007-2014

Walker, R. T., Parizek, B. R., Alley, R. B., Anandakrishnan, S., Riverman, K. L., & Christianson, K. (2013). Ice-shelf tidal flexure and subglacial pressure variations. *Earth and Planetary Science Letters*, *361*, 422–428. https://doi.org/10.1016/j.epsl.2012.11.008

Warburton, K. L. P., Hewitt, D. R., & Neufeld, J. A. (2020). Tidal grounding-line migration modulated by subglacial hydrology. *Geophysical Research Letters*, *47*(17). https://doi.org/10.1029/2020GL089088

Wild, C. T., Marsh, O. J., & Rack, W. (2019). Differential interferometric synthetic aperture radar for tide modelling in Antarctic ice-shelf grounding zones. *The Cryosphere*, *13*(12), 3171–3191. https://doi.org/10.5194/tc-13-3171-2019

Xie, S., Dixon, T. H., Voytenko, D., Deng, F., & Holland, D. M. (2018). Grounding line migration through the calving season at Jakobshavn Isbræ, Greenland, observed with terrestrial radar interferometry. *The Cryosphere*, *12*(4), 1387–1400. https://doi.org/10.5194/tc-12-1387-2018